

Timing Optimisation and Analysis in the Design of 3D silicon sensors: the TCoDe Simulator

Angelo Loi,^a Andrea Contu,^a Adriano Lai,^{a,1}

^a*Istituto Nazionale Fisica Nucleare, Sezione di Cagliari, Cagliari, Italy*

E-mail: adriano.lai@ca.infn.it

ABSTRACT: Solid state sensors having timing capabilities are becoming an absolute need in particle tracking techniques of future experiments at colliders. In this sense, silicon sensors having 3D structure are becoming an interesting solution, due to their intrinsic speed and radiation resistance. A characteristics of such devices is the strict dependence of their performance on their geometric structure, which can be widely optimised by design, thus requiring suitable tools for an accurate modeling of their behaviour. This paper illustrates the development, performance and use of the TCoDe simulator, specifically dedicated to the fast simulation of carrier transportation phenomena in solid state sensors. Some examples of its effectiveness in the design and analysis of 3D sensors is also given.

KEYWORDS: Timing detectors, Detector modelling and simulations II (electric fields, charge transport, multiplication and induction, pulse formation, electron emission, etc)

¹Corresponding author.

Contents

1	Introduction	1
2	Solid state sensors for timing	2
2.1	Characteristics of 3D silicon sensors and timing	3
3	Analysis of static properties and 3D silicon sensor design	3
3.1	Technology and starting design criteria	3
3.2	2D geometry study: the Ramo maps	4
3.3	3D design	6
4	Simulation of carrier dynamics and signal generation: the TCoDe software	8
4.1	Energy deposits	9
4.2	Sensor geometry and physics maps	9
4.3	Carrier motion	9
4.4	Carrier diffusion for thermal effects	10
4.5	Induced current	10
4.6	Multithread implementation	11
5	Timing behaviour of 3D silicon sensors	11
5.1	Comparison between timing performance of different 3D structures	12
5.2	Study of measured timing performance	14
6	Conclusions	14

1 Introduction

Tracking systems of the next-to-come high-energy physics experiments at colliders, and vertex detectors in particular, will have to cope with a hugely increasing number of tracks per collision to be processed. The logical solution to this experimental challenge is to associate a precise measurement of the time coordinate to the tracking hits. This solution has been pioneered by the NA62 experiment, with resolutions around 150 ps [3] per hit, and already adopted for the tracking systems of the Phase-II Upgrades of the ATLAS and CMS experiments at the Large Hadron Collider (LHC), where dedicated *Timing Layers* [8, 10], aiming at resolutions round 30 ps per track are currently under development. In the high-luminosity Upgrade-2 of the LHCb experiment [18, 19], planned for the Run 5 of the LHC, this requirement is even more demanding, because, in order to ensure satisfactory track reconstruction efficiency, the timing information is needed at the single pixel level of the vertex detector. Similar and more stringent conditions are expected for the next generation of colliders, that is those of the so-called *Future Circular Collider* family [5, 9, 14].

This experimental approach concerns the detector system as a whole (from sensors to the front-end electronics and the processing stage). In this sense, the TIMESPOT Project aims at developing a full tracker demonstrator of reduced size (a few thousand channels and 4 to 5 tracking planes), making thus possible to conceive the single system constituents considering also the inter-relationship and inter-connections of its single parts, from the sensor to the reconstruction algorithms [11]. The development of very rad-hard and high-resolution sensors is a starting and crucial passage of such systems. Required time resolutions are in the range of at least 50 ps per hit [20], which have to be maintained up to and beyond very high particle fluences (larger than 10^{16} n_{eq}/cm² (1 MeV neutron equivalent/cm²)).

The TIMESPOT collaboration has already developed dedicated sensors for timing, which demonstrated to reach excellent time resolution, in the range of 15-20 ps [7]. This paper illustrates the conception and operation of a custom simulation tool, named TCoDe (TIMESPOT Code for Detector simulation), which has played a crucial role in the design and detailed simulation of the sensors produced, making it possible to fully characterise the sensor models with very high statistics within reasonable processing times. For similar reasons, TCoDe is also very useful in a detailed study and interpretation of the measured sensor behavior. The paper is organised as follows. Section 2 recalls some basic principles about time resolution in silicon sensors. Section 3 illustrates the relevant design parameters in defining the sensor simulation model and the main steps in sensor design. Section 4 describes the conception and operation of the TCoDe software, while section 5 illustrates some examples of its practical usage. Finally, section 6 draws our conclusions.

2 Solid state sensors for timing

In a generic silicon sensor, it is possible to summarise the main contributions to time resolution σ_t by means of the formula:

$$\sigma_t = \sqrt{\sigma_{ej}^2 + \sigma_{tw}^2 + \sigma_{un}^2 + \sigma_{dr}^2 + \sigma_{TDC}^2}, \quad (2.1)$$

where σ_{ej} is the electronic jitter, depending on electronic noise and pre-amplifier speed; σ_{tw} are the time-walk fluctuations, depending on different times of discriminator threshold crossing of signals with same shape and different amplitudes; σ_{dr} is due to the time fluctuations due to delta-rays deposits during the ionisation process; σ_{TDC} depends only on the Time-to-Digital-Converter resolution. The term σ_{un} (field unevenness) is strictly related to the uniformity in the weighting field and drift velocity across the sensor volume, as established by the Ramo theorem [24], giving an induced current $i(t, \mathbf{r}) = q \mathbf{E}_w \cdot \mathbf{v}_d$, where q the carrier charge, \mathbf{E}_w the weighting field and \mathbf{v}_d the carrier drift velocity. $i(t, \mathbf{r})$ is the induced current signal at a given space-time point inside the sensor volume, during the drift time of the generated charge carriers (electrons and holes). We call $i(t, \mathbf{r})$ as *i-let*, being the elementary contribution to the current signal at the sensor electrodes. This concept will be exploited in the following (see section 3).

Among the contributions in eq. 2.1, the term σ_{ej} depends both on sensor (sensor noise) and electronics, the terms σ_{tw} and σ_{TDC} are independent of the sensor, while σ_{dr} and σ_{un} depend only on the sensor geometry and therefore can be optimised by design for fast timing.

2.1 Characteristics of 3D silicon sensors and timing

Silicon sensors based on 3D electrode geometry were proposed more than two decades ago by S. Parker [22, 23]. Unlike their planar counterpart, the electrode structure of 3D silicon sensors is developed in the vertical direction, orthogonal to their surface. At the expenses of a more complex production process, this structure bears a number of important advantages. As the sensor thickness is made independent of the inter-electrode distance, the charge carrier drift length can be made very short (around 20-30 μm), and the induced current signals very fast, while preserving the amount of charge deposited by ionisation inside the sensor volume, and therefore the signal amplitude.

The vertical electrodes roughly follow the path of the ionising particle to be detected. This makes the effect of delta rays (σ_{dr} in eq. 2.1) on time fluctuations negligible, improving time resolution. It is worth recalling here that delta rays, sometimes referred to as *Landau fluctuations*, pose an intrinsic limit to the time performance of other silicon sensors based on timing-optimised planar technology [26].

The short inter-electrode distance has also a beneficial effect on radiation hardness, as reduces the trapping probability of the charge carriers while they travel towards the collecting electrodes. Indeed, 3D silicon sensors show an unmatched radiation resistance, being successfully tested up to $3 \times 10^{16} \text{ n}_{\text{eq}}/\text{cm}^2$, still without reaching their operation limit [17].

Because the σ_{dr} term is naturally at its minimum, in 3D silicon sensors the term σ_{un} is crucial for the improvement of timing performance. It depends strongly on the geometrical structure of the sensor sensitive volume. Once the velocity saturation regime is reached, the more uniform the weighting field, the more uniform the shape of the signals and consequently the smaller the time arrival dispersion. On the other hand, the sensor contribution to the noise, affecting the term σ_{ej} , also depends on the geometry of the sensor volume through its capacitance and therefore must be carefully considered during the design optimisation process.

3 Analysis of static properties and 3D silicon sensor design

Once the specific technology and sensor pitch are chosen, the timing optimisation and detailed design of 3D silicon sensors starts with an accurate definition of the pixel geometrical structure. In this first stage, the so-called *static properties* of the pixel are studied and defined. These are those physical properties which fix the operating conditions of the sensor, that is the electric field, the weighting field and the carrier velocities. The *static properties* strictly depend on the electrode structure and on the bias voltage and correspond to well defined value maps across the whole sensor volume. They establish the playground where the carrier dynamics and signal generation are then simulated and characterised.

The study of the *static properties* has been entirely performed by means of the Synopsys Sentaurus TCAD [27] software.

3.1 Technology and starting design criteria

The 3D sensors which have been designed were to be fabricated using a Single-Sided (Si-Si) fabrication approach and the Deep Reactive Ion Etching (DRIE) process [15]. The Si-Si rather than the double-sided technology, which was used for the ATLAS-IBL 3D sensors [2, 13], allows

using a thick support wafer directly bonded to the high-resistivity device layer, so as to improve the mechanical stability of wafers during fabrication and reduce wafer bowing due to mechanical stresses during production. In this way sensitive layers as thin as $150\ \mu\text{m}$ and electrodes having diameter (column shapes) or width (trench shapes) of about $5\ \mu\text{m}$ can be fabricated. These values have been adopted as reference minimum sizes in our design. Figure 1 shows a schematic of the Si-Si structure. On the other hand, the $150\ \mu\text{m}$ sensitive silicon depth, still provides a Most Probable Value (MPV) of 2 fC charge deposit, which appears sufficient for our purposes, as will be demonstrated in the following sections. The pixel size is kept on a pixel pitch of $55\ \mu\text{m}$ in order to

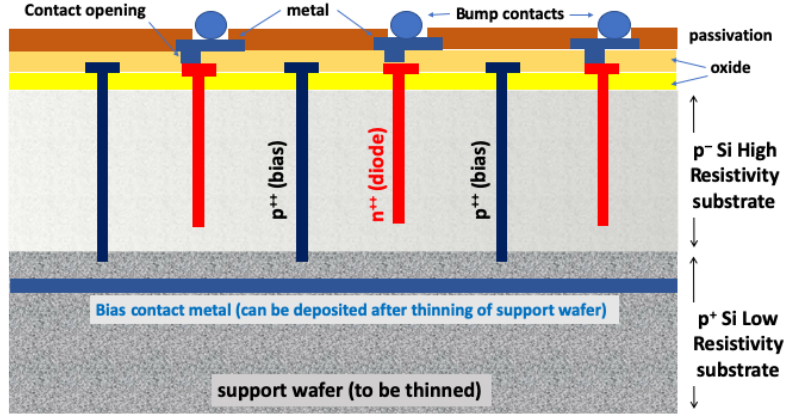


Figure 1. Schematic of the internal structure of a 3D silicon sensor in Single-Sided technology.

be compatible with the TIMEPIX ASIC family [21]. This choice was done uniquely for practical reasons, to have additional chances in testing the pixel matrices produced.

As stated in section 2, the basic criteria for timing optimisation consists in obtaining maximally uniform and high values of the i -let contributions to the induced current signal

$$i(t, \vec{r}) = q \vec{E}_w \cdot \vec{v}_d \quad (3.1)$$

Uniform sensor response is achieved by operating the sensor at sufficient high bias voltages so as to generate electric fields of magnitude greater than $10\text{kV cm}^{-1}\text{m}$ necessary to accelerate electrons and holes to velocity saturation. In 3D silicon sensors relatively low bias voltages are sufficient to achieve the saturated velocity regime, as shown in the example given in Figure 2.

The second ingredient of fast sensor response is the weighting field \vec{E}_w , which couples the current induction over the entire active volume with the sensor geometry and is, therefore, only dependent on the chosen electrode shape. The crucial role of the weighting field is further considered in the following subsection.

3.2 2D geometry study: the Ramo maps

The first step of sensor design is a preliminary study performed in order to define a limited group of geometries potentially suited for fast timing. This step is based on bi-dimensional quasi-stationary TCAD simulations (named 2D-TCAD). It consists in designing a vertical cut of the pixel in different

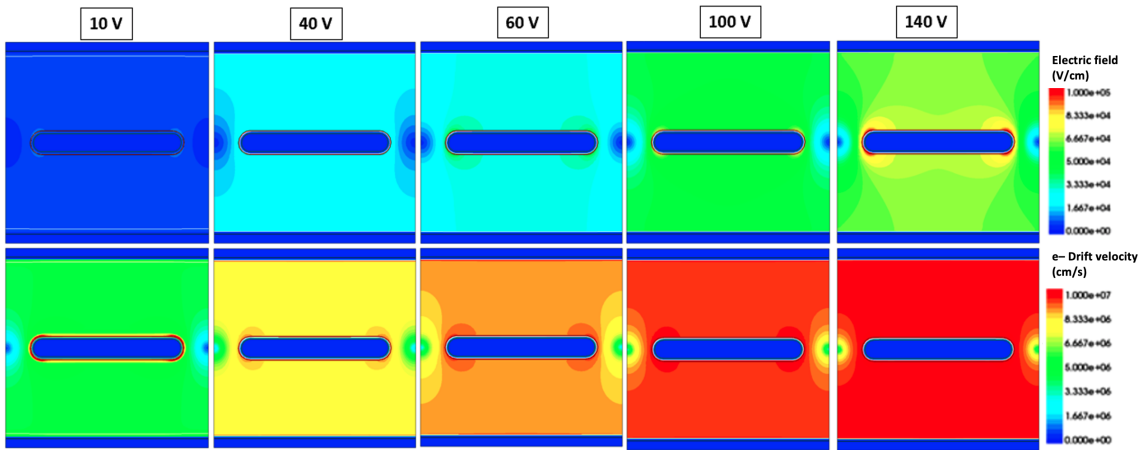


Figure 2. Electric field and electron drift velocity with increasing bias voltage. At 100 V the electric field is sufficiently high to guarantee velocity saturation over the entire active area.

electrode geometries, according to its 3D symmetry. This 2D model of the device is simulated with increasing bias voltage and its relevant physics properties are characterised at a temperature of 300 K and an inverse bias voltage of 100 V. This voltage is considered as a good reference to immediately exclude geometries where drift velocity is still below saturation regime in some specific areas. During this first step, different electrode geometries are designed, simulated and evaluated, featuring different combinations of square and hexagonal pixels with trench or column electrodes.

Within the 2D-TCAD study, a new approach was developed to better identify electrode geometries for fast timing applications. The method, based on the Ramo theorem, is called *Ramo map* and consists in building a 2D map of the electron or hole *i-let* values across the area. The Ramo map shows directly how strong and uniform a single carrier current induction is in a specific electrode geometry, allowing in this way to identify critical spots and the potential single carrier output swing of the sensor.

A Ramo map is generated starting from the 2D model of an entire 3×3 pixel matrix (figure 3). The innermost pixel is the pixel under study and is called *Pixel of Interest* or PoI. The other boundary pixels are needed to better describe the weighting field of the PoI. A first quasi-stationary simulation is performed with normal operational voltages and is needed to compute the drift velocity maps of the device. A second quasi-stationary simulation is used to compute the weighting field. In this case the boundary conditions have a potential $V = 0$ on all the electrodes but the readout electrode of the PoI, which is set to $V = 1$. Weighting field and drift velocity maps are then scalar-multiplied point by point over the entire area according to the Ramo theorem (figure 4).

The Ramo map gives a first quantitative estimate of the degree of timing performance of a given 3D sensor geometry. An ideal Ramo map bears uniform and high *$\tilde{A}n-let$* values. This approach allows saving time during geometry pre-selection, so to devote more time on the final design with more detailed and time-consuming 3D-TCAD simulations.

Figure 5 shows a comparison among three different electrode geometries by means of their Ramo maps generated at the same bias voltage of $V = -100$ V and 300 K. Among all different geometries, those with a parallel configuration of their electrodes present the highest current

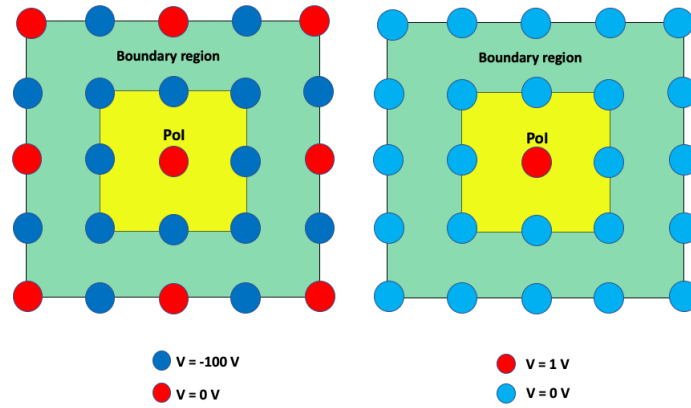


Figure 3. Boundary conditions for a Ramo map: Left: boundary conditions for quasi stationary device simulation needed to compute drift velocity maps. Right: boundary conditions for the weighting field.

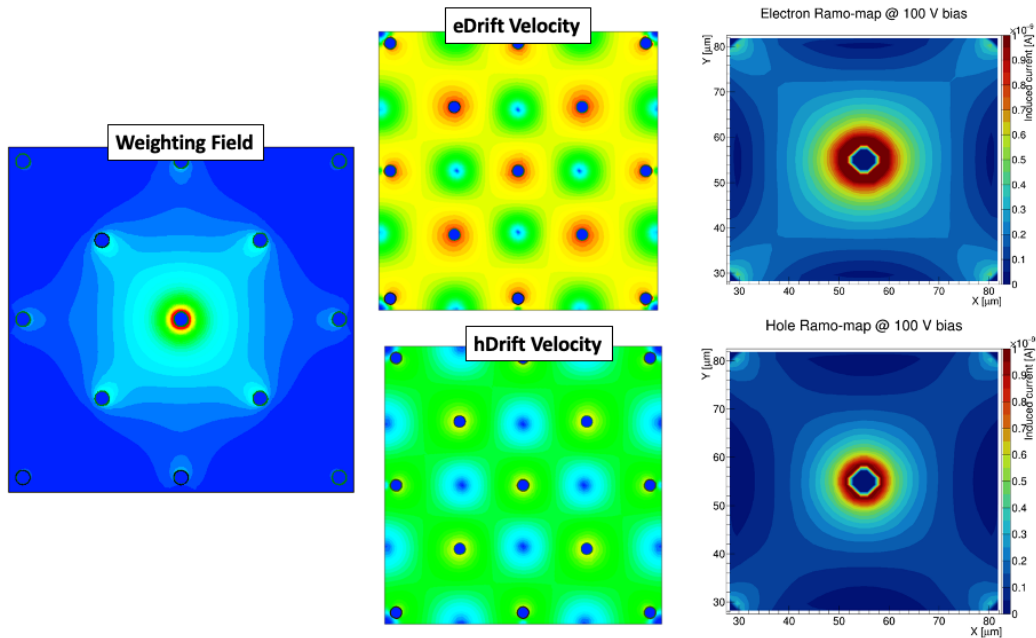


Figure 4. Ramo map generation for a 5-column squared geometry from the calculation of the weighting field and carrier velocity maps.

induction with the smallest output current swing. The parallel trench electrode geometry shows the best characteristics. More classic geometries like the 5-column pixel device, used in the ATLAS-IBL or considered for the ATLAS ITK, presents $\tilde{A}n\text{-let}$ values which are lower in most of the sensor area. Moreover, they are less uniform and consequently give a much larger output current swing.

3.3 3D design

After geometry selection, a complete 3D model is designed and simulated, featuring more details of the fabrication process like the $20\ \mu\text{m}$ shorter junction electrode with respect to the ohmic ones,

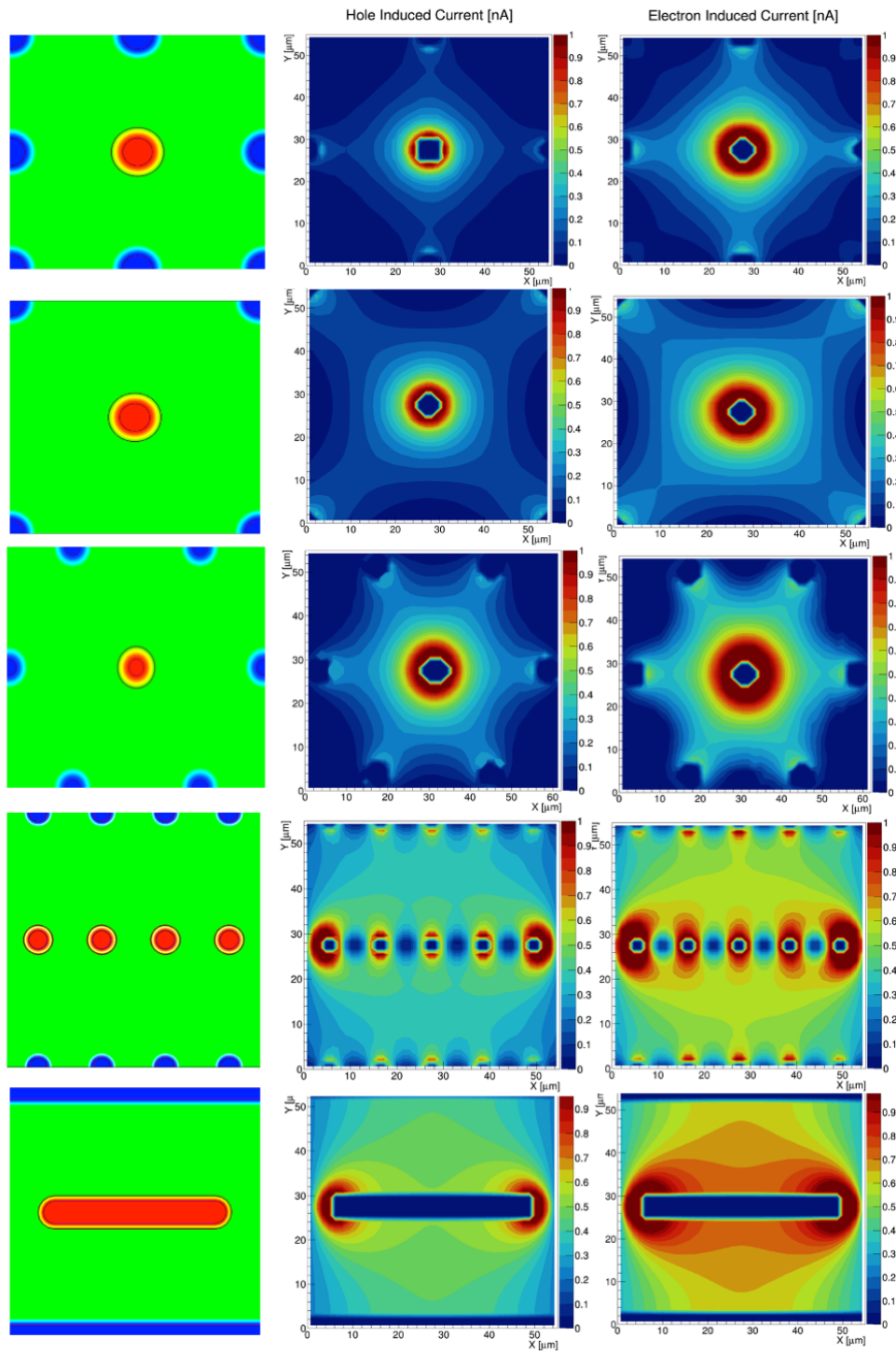


Figure 5. Ramo map comparison of five different electrode geometries. From left to right: doping profiles (red: n++ doping, blue: p++ doping), hole Ramo map, electron Ramo map. From top to bottom: squared 9-columns, squared 5-columns, hexagonal 7-columns, parallel 12-columns, parallel trench.

a p-spray layer on top of the pixel in order to increase radiation hardness against superficial damage and a thin layer of low resistive and p++ doped silicon layer from the support wafer which is left after the fabrication process, providing bias from the bottom (see figure 6). Detailed simulations of the model are performed in order to have a more detailed overview of the real device, estimate its capacitance using small AC signal analysis and generating the physics needed to perform transient simulation using the TCoDe fast transient simulator. For such a purpose, the complete 3D model outputs 3D maps of the electric field, carrier mobilities and weighting field. The structure and operation of the TCoDe simulator is described in the next section.

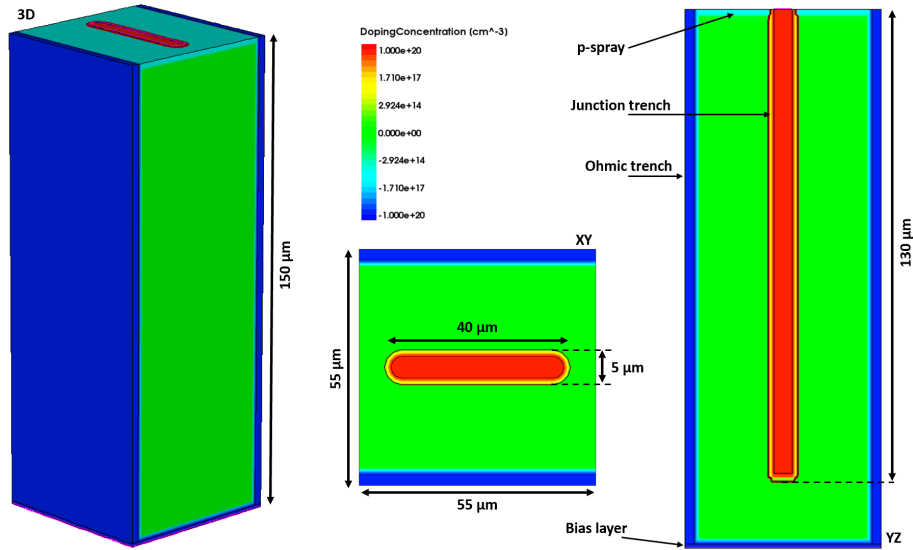


Figure 6. 3D rendering of the TIMESPOT parallel trench device showing doping concentration and internal structure. Radiation hardness along the surface is increased using a p-spray layer. The bottom of the sensor presents the residual layer of the support wafer which is used to provide the bias voltage to the ohmic electrodes.

4 Simulation of carrier dynamics and signal generation: the TCoDe software

TCoDe [12] (TIMESPOT Code for Detector simulation) is a C++14 –compliant application to simulate the response of solid state sensors in massively parallel platforms on Linux systems. TCoDe is implemented on top of Hydra [6] and as such, it can run on OpenMP, CUDA and TBB compatible devices.

TCoDe uses external 3D maps of electric fields, carrier mobilities, weighting field and energy deposit to simulate the response in current of solid state sensors. The motion of the individual carriers produced in the initial deposit is determined with a 4th order Runge–Kutta algorithm using electric field and mobility maps and assuming that the carriers always move at drift velocity. At each time interval the current induced in the electrode is calculated from the carriers velocity using the corresponding weighting field, according to the Shockley-Ramo theorem. The output is stored to ROOT [1] files, several level of output detail are available, from the simple current vs time plot to the complete information about the position of the carriers at each time step.

4.1 Energy deposits

TCoDe is able to generate its own energy deposits or import them from other tools like GEANT4 [4]. The deposit is determined by its energy, E_{dep} , released along a path of length l , identified by the start and end point of the ionization path ($(X_i; Y_i; Z_i)$ and $(X_f; Y_f; Z_f)$), the energy deposit E_{dep} , the dispersion of the charges at the beginning α_i and end α_f of the path. Distinction between primary and secondary contributions, such as δ rays is also possible. In this latter case, the deposit is composed by several straight segments. The carriers distribution is created by converting these straight energy deposits into an equivalent number of electron-hole pairs. This operation is performed by dividing the energy deposit by the average energy needed to generate an electron hole pair which, in case of silicon, is equal to 3.6 eV. At the end of the process there will be a number of point-like carriers, N_{max} , distributed in space.

4.2 Sensor geometry and physics maps

TCoDe is sensor-agnostic, in the sense that there is no assumption on the shape or its features. The sensor is entirely defined by physical quantities, or maps, provided across the sensor volume: electric field vector, electron and hole mobilities, weighting field. To be more efficient in the calculations these quantities have to be provided in points on a 3D grid, not necessarily a regular one, to allow a fast lookup via binary search, depending on the carrier position. The grid does not have to be the same for all physical quantities, although if this is true, the calculation will be faster. If the physics maps are not provided in this format, they will have to be converted through interpolation. In general a carrier will not sit exactly on one of these grid points, but it will be in a position surrounded by 8 of them so that the physical quantities can easily be calculated through a simple linear interpolation. Since physics maps can be very large depending on the sensor, some optimisation is required, for example by using a coarser grid in regions where the quantities vary slowly. However the size of the grids (and therefore their level of refinement) has to be decided depending on the hardware available, there is no limitation coming from the TCoDe software. Physics maps used in this paper have roughly 1M points and are a few giga-bytes large.

4.3 Carrier motion

The motion of each carrier is treated separately and interaction among them is neglected. This can generally be assumed for 3D sensors since there is no multiplication and therefore the charge density is sufficiently low. Charge drift is computed by solving the following differential equation which describes charge motion in semiconductors under effects of an electric field:

$$\frac{\delta \vec{r}_d}{\delta t} = \mu \vec{E} \quad (4.1)$$

As integration method the Runge–Kutta 4th order algorithm was implemented. The algorithm computes for the time step N the drift motion step \vec{r}_{dN+1} .

$$\vec{r}_{dN+1} = \vec{r}_{dN} + \frac{\Delta t}{6}(k_1 + 2(k_2 + k_3) + k_4) \quad (4.2)$$

With $k_{1,2,3,4}$ the Runge–Kutta parameters, which are:

$$\begin{cases} \vec{k}_1 = \mu_{e,h}(t_n, \vec{r}_{dN}) \vec{E}(t_n, \vec{r}_{dN}) \\ \vec{k}_2 = \mu_{e,h}(t_n + \frac{t_{step}}{2}, \vec{r}_{dN} + \frac{1}{2} \vec{k}_1 t_{step}) \vec{E}(t_n + \frac{t_{step}}{2}, \vec{r}_{dN} + \frac{1}{2} \vec{k}_1 t_{step}) \\ \vec{k}_3 = \mu_{e,h}(t_n + \frac{t_{step}}{2}, \vec{r}_{dN} + \frac{1}{2} \vec{k}_2 t_{step}) \vec{E}(t_n + \frac{t_{step}}{2}, \vec{r}_{dN} + \frac{1}{2} \vec{k}_2 t_{step}) \\ \vec{k}_4 = \mu_{e,h}(t_n + \frac{t_{step}}{2}, \vec{r}_{dN} + \frac{1}{2} \vec{k}_1 t_{step}) \vec{E}(t_n + h, \vec{r}_{dN} + \vec{k}_1 t_{step}) \end{cases} \quad (4.3)$$

The electric field \vec{E} and mobility $\mu_{e,h}$ are extracted or interpolated from the input physics maps.

4.4 Carrier diffusion for thermal effects

Finite temperature adds a random component to the carrier motion. This is quantified by the diffusion coefficient D which depends on the temperature of the silicon

$$D = \frac{k_B T}{e} \mu_{e,h}, \quad (4.4)$$

where k_B is the Boltzmann constant and $\mu_{e,h}$ are the electron (hole) mobility which is directly taken from the mobility maps. For a time step Δt the path traveled by the charge is equal to

$$\sigma_{diff} = \sqrt{2D\Delta t} \quad (4.5)$$

Diffusion direction is a completely random process and for every time step its direction and distance varies randomly. In order to include this aspect in the simulation, σ_{diff} is computed as the variance of a random number generator with Gaussian distribution with mean value 0. This allows to compute for every Δt a random drift distance within the desired distribution. The orientation of the diffusion step is also randomly computed by rotating the vector of length σ_{diff} around the origin with an angle θ and ϕ .

$$\delta \vec{r}_{diff} = \begin{pmatrix} X_{diff} \\ Y_{diff} \\ Z_{diff} \end{pmatrix} = \begin{pmatrix} \cos(\phi) \sin \theta & -\sin(\phi) & -\cos(\phi) \sin \theta \\ \sin(\phi) \cos \theta & \cos(\phi) & -\sin(\phi) \cos \theta \\ \sin(\theta) & 0 & \cos \theta \end{pmatrix} \times \begin{pmatrix} \sigma_{diff} \\ \sigma_{diff} \\ \sigma_{diff} \end{pmatrix} \quad (4.6)$$

With θ and ϕ randomly generated angles between $[-\pi, \pi]$ and $[0, 2\pi]$ respectively. $\delta \vec{r}_{diff}$ is simply added to the carrier motion due to the electric field. At the end of the time step, \vec{r}_{dN+1} and $\delta \vec{r}_{diffN+1}$ are added together to obtain the total distance travelled by the charge:

$$\vec{r}_{N+1} = \vec{r}_{dN+1} + \vec{r}_{diffN+1} \quad (4.7)$$

4.5 Induced current

The current induced on the electrode is calculated by applying the Ramo theorem

$$i_{e,h} = q_{e,h} (v_{x_{e,h}} E_{w_x} + v_{y_{e,h}} E_{w_y} + v_{z_{e,h}} E_{w_z}), \quad (4.8)$$

where $E_{w_{x,y,z}}$ is the weighting field at the position of the carrier. The contribution of every single charge is added at the end of each time step and saved on the output file. In default settings the output includes the time step, the total induced current in time and integrated charge in time. It is

also possible to save the contributions of the electrons and holes separately, as well as the charge generated by primary and secondary particles. In this way, it is possible to analyze the contribution of electrons and holes separately or the contribution from deposits generated by primary or secondary particles. Moreover, it is possible to save the drift path of every single charge and use the data to visualise the entire process.

4.6 Multithread implementation

The characteristics of TCoDe is to have the ability to perform very detailed simulations, by following each carrier individually, but at the same time being extremely fast thanks to its multithread implementation. Parallelization is used whenever possible in the code, however most of the performance comes from treating all the carriers simultaneously so that each time step bunches of carriers can be processed in parallel. TCoDe can parallelize both in CPU (OMP, TBB), or NVIDIA GPU (CUDA). In general, it supports all backends supported by Hydra, on top of which TCoDe is built. It is clear that the performance depends strictly on the number of parallel threads and therefore on the hardware available. Moreover, all calculations are performed in double precision. As it is now, TCoDe cannot simulate sensors where charge multiplication occurs. This is because if the number of carriers changes, then also the number of threads should. There are ways to overcome this issue, for example by grouping carriers, but this is not yet fully implemented. Given a set of physics maps and a certain hardware, there are two parameters of the simulation that allow to reach the best compromise between detail and performance: these are the number of carriers and the time step. The user has to find the best compromise between these two. As an extra handles, charges can be treated in groups, so that the effective number of threads is reduced by the size of the groups.

Typical performances on consumer desktop and laptop computers are reported on Table 1. It

Backend	Simulation time [sec]	
	Desktop PC	Laptop
Single thread	24.5	29
TBB	5.3	6.8
OMP	5.6	8.4
CUDA	1.3	3.5

Table 1. Calculation time for a simulated MIP deposit of 12000 hole-electron pairs in the parallel trench sensor. A total of 2000 1ps time steps are executed. The timing is shown for a desktop pc (Intel Core i7-6700K processor, 16 GB RAM and an NVIDIA GeForce GTX 1080) and a laptop (Intel Core i7-7700HQ, 16 GB RAM and an NVIDIA GeForce GTX 1050).

is noted that since double precision is required, only double precision cores are used in GPUs. Therefore, performances are expected to improve significantly on professional GPU cards.

5 Timing behaviour of 3D silicon sensors

In the present section we illustrate two examples of design and data analysis methodologies using the TCoDe simulator. In the first case (subsection 5.1), TCoDe is used on full size 3D pixel models to perform a detailed study concerning the timing performance foreseen for 3D sensors according

to their geometries. In the second case (subsection 5.2) TCoDe shows its potentiality in studying and understanding the timing behavior sensors already tested in the laboratory.

5.1 Comparison between timing performance of different 3D structures

The TCoDe simulator is used here to compare the timing performance of four different 3D geometries. As performance indicator we will use the charge collection time (CCT) distribution. The CCT is defined as the time needed for all the carriers generated by a given track to reach their respective electrodes, that is for the induced current signal to return to zero. As widely demonstrated in [16], the CCT distribution can be strictly correlated with the final time resolution of the detecting system in such a way to create a direct connection between the standard deviation σ_{t_c} of the CCT distribution and the one of the time of the arrival distribution σ_t . The four geometries under comparison are shown in figure 7.

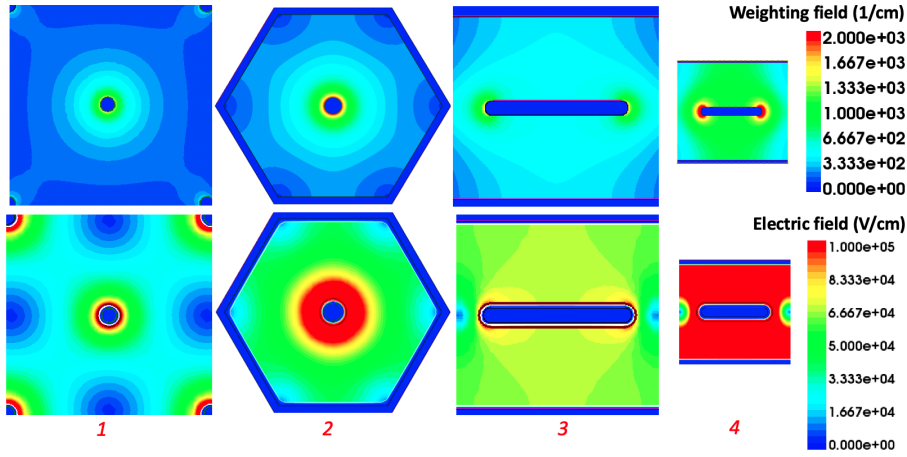


Figure 7. Transverse cuts of 3D pixels with different geometries. Weighting field maps (top row) and Electric field maps (bottom row) at $V_{bias} = -150V$. Geometries 1 to 3 have pitch = $55\mu m$, while 4 has pitch = $25\mu m$. TCAD simulations.

The Ramo maps of the four geometries are reported in figure 8. It can be already noticed that the trench geometries provide much more uniform and higher i_{let} values. This fact suggests that the 3D-trench geometry will have higher induced current signals, shorter signal time, faster charge collection and, consequently, better time resolution.

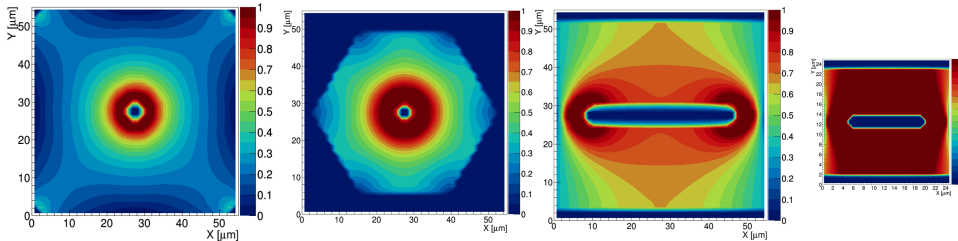


Figure 8. Electron Ramo map comparison for the four 3D geometries of figure 7.

To explore the time response of the different sensor geometries, a TCoDe simulation is performed. The simulation is obtained by analysing the effect of about 2 500 MIP perpendicular tracks, scanning completely the area of each type of sensor in steps of $\approx 1\mu\text{m}$. The result is illustrated in figure 9, which represents the simulated CCT for each point of the pixel area. The CCT maps allows also an immediate and detailed check about the *weak spots* inside the pixel volume.

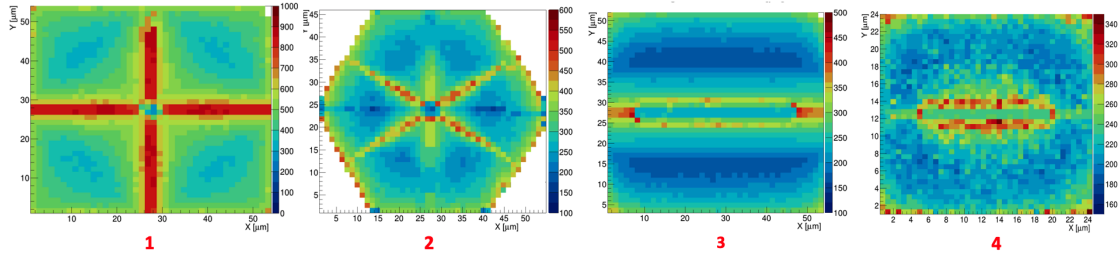


Figure 9. TCoDe-simulated 2D-maps of Charge Collection Times [ps] for four different geometries (1-4) reported in figure 7. Please note the different scales in the color code.

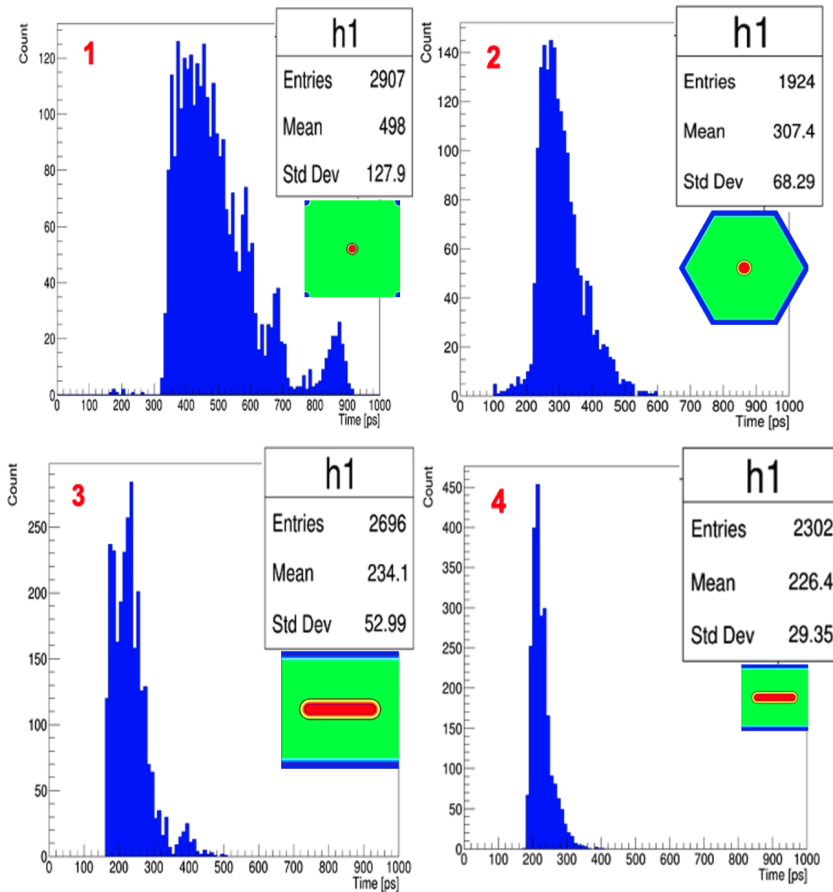


Figure 10. TCoDe-simulated distributions of Charge Collection Times [ps] for the geometries (1-4) of figure 7 to 9 (see insets).

A further step of this analysis is getting the CCT distributions which sum-up the internal contributions of the whole pixel. These are given in figure 10. From the obtained distributions we can basically extract two characteristic parameters: the mean CCT or *time centroid* [25] of the pixel, or t_c , and the standard deviation, or σ_{t_c} , which can give useful predictions on the final time resolution of the system, being [16]

$$\sigma_t = P\sigma_{t_c}, \quad (5.1)$$

where P is called *timing propagation coefficient* and is a function of the front-end characteristics. Such final analysis goes beyond the scope of the present work. We can limit to observe the effectiveness of the TCoDe analysis in describing and predicting the time behaviour of sensors and in particular of the 3D technology sensors. Moving from the 3D-column geometry (number 1) to the parallel trench geometry (number 3) provides more than a factor 2 gain in σ_{t_c} . Pitch reduction (geometry number 4) can almost double the effect.

5.2 Study of measured timing performance

As shown in the previous section, TCoDe can be used to realise virtual and controlled experiments on sensors, which can allow an almost one-to-one comparison with measurements. Starting from the detailed description of the current signals as induced at the electrodes $i(t)$ and considering the front-end transfer function $H(t)$, it is possible to obtain the front-end response by the convolution

$$v_{out}(t) = i(t) * H(t). \quad (5.2)$$

The distribution of the time of arrivals of the $v_{out}(t)$ signals can then be built by applying a suitable discrimination algorithm. Figure 11 (left) gives the simulated distributions of the Time of Arrivals (ToA) of the $v_{out}(t)$ signals. The time of arrival (ToA) of each signal was obtained by applying a constant fraction discriminator with threshold at 35% of signal amplitude. The simulated ToA distribution is compared in figure 11 to a ToA distribution coming from test-beam measurements (left) [7]. The simulated behavior qualitatively well corresponds to the measured one. To obtain a more sticking and quantitative comparison, an accurate modeling of the front-end and of its noise behaviour is still needed.

TCoDe can be used to accomplish a dedicated study of the ToA distribution structure of the type shown in figure 11. This can be analysed by distinguishing the contributions to the time distribution per different pixel areas. Figure 12 reports such analysis and indicates the correspondence between the single sub-distributions and pixel sub-areas. The plot points out clearly the sub-areas which slow down the global performance and can suggest suitable modifications in the pixel geometry to further optimise its time resolution.

6 Conclusions

The present work describes the structure and functionalities of the TCoDe simulator. It is released with a *GPLv3* license and its open-source code can be found and downloaded at the link indicated in [12]. Some examples have been given about the TCoDe effectiveness in the design of 3D silicon sensors, when coupled to other tools for electric field description, as well as in the analysis and interpretation of data from measurements. Although its development is mainly dedicated to

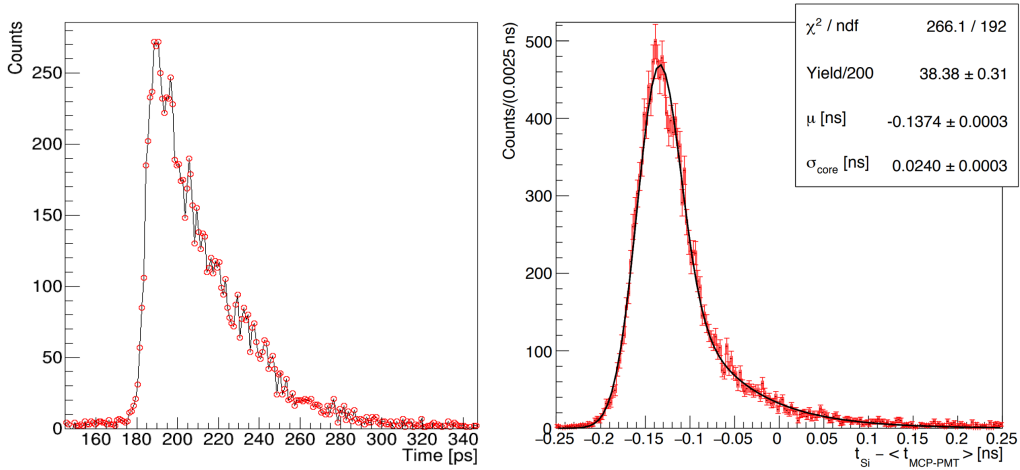


Figure 11. Simulated (left) and measured (right) distributions of ToA for a 3D-trench sensor.

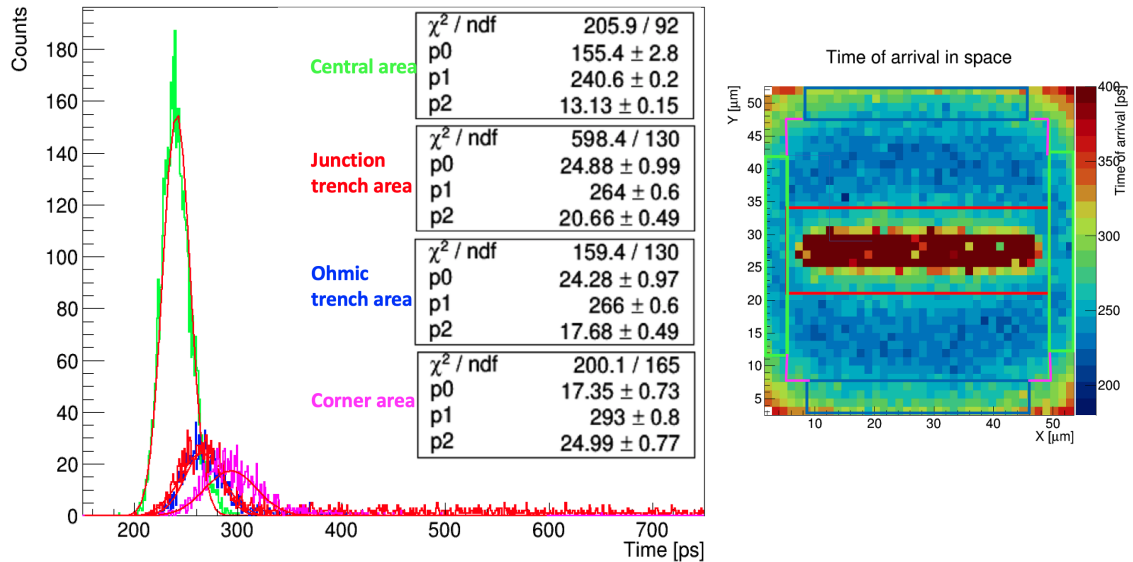


Figure 12. Decomposition of the ToA distribution of figure 11 (left) according to different pixel areas (right).

3D silicon sensor modeling, TCoDe is not technology-specific and is easily transportable to the modeling of the carrier transportation mechanisms of any solid state sensor. In particular, its multi-thread core makes perfectly feasible to realize full-scale virtual experiments in reasonable time and on medium-level machines (see Table 1), where other methods are simply impractical solutions even whether used on high-end computing infrastructures.

Acknowledgments

This work was supported by the Fifth Scientific Commission (CSN5) of the Italian National Institute for Nuclear Physics (INFN), within the Project TIMESPOT and by the ATTRACT-EU initiative,

INSTANT project. The authors are grateful to Gian Matteo Cossu for his help in providing the front-end transfer function used in figures 11 and 12.

References

- [1] <https://root.cern>, 2020.
- [2] B. Abbot et al. Production and integration of the ATLAS Insertable B-Layer. *JINST*, 13:T05008, 2018. doi: 10.1088/1748-0221/13/05/t05008.
- [3] G. Aglieri-Rinella et al. The NA62 GigaTracker. *Nuclear Instruments and Methods A*, 845:147–149, feb 2017. doi: 10.1016/j.nima.2016.06.045. URL <https://doi.org/10.1016/j.nima.2016.06.045>.
- [4] S. Agostinelli et al. Geant4: A simulation toolkit. *Nucl. Instrum. Meth.*, A506:250, 2003. doi: 10.1016/S0168-9002(03)01368-8.
- [5] M. Aleksa et al. Strategic rd programme on technologies for future experiments. *Tech. Rep. CERN-OPEN-2018-006*, CERN, Geneva, 2018. URL <https://cds.cern.ch/record/2649646>.
- [6] A. Alves Junior. MultithreadCorner/Hydra, 2020. URL <https://doi.org/10.5281/zenodo.1206261>.
- [7] L. Anderlini et al. Intrinsic time resolution of 3D-trench silicon pixels for charged particle detection. *Journal of Instrumentation*, 082:P0420, 4 2020.
- [8] ATLAS Collaboration. Technical Proposal: a High-Granularity Timing Detector for the ATLAS Phase-II Upgrade. *CERN-LHCC-2018-023*, *LHCC-P-012*, 2018.
- [9] CEPC Study Group. CEPC Conceptual Design Report. *arXiv:1809.00285*, 2018.
- [10] CMS Collaboration. A MIP Timing Detector for the CMS Phase-2 Upgrade. Technical Design Report. *CERN-LHCC-2019-003*, *CMS-TDR-020*, 2019.
- [11] T. collaboration. web site: <https://web.infn.it/timespot/index.php>, 2020.
- [12] A. Contu and A. Loi. MultithreadCorner/TCode, 2020. URL <https://doi.org/10.5281/zenodo.3686010>.
- [13] C. Da Via et al. 3D silicon sensors: Design, large area production and quality assurance for ATLASIBL pixel detector upgrade. *Nucl. Instrum. Meth. A*, 694:321–330, 2012.
- [14] FCC Collaboration. The Future Circular Collider (FCC) Conceptual Design Report. *CERN-ACC-2018-0056*, *CERN-ACC-2018-0057*, *CERN-ACC-2018-0058*, *CERN-ACC-2018-0059*, 2018.
- [15] F. Laermer, S. Franssila, L. Sainiemi, and K. Kolari. Chapter 21 - deep reactive ion etching. In M. Tilli, T. Motooka, V.-M. Airaksinen, S. Franssila, M. Paulasto-KrÄckel, and V. Lindroos, editors, *Handbook of Silicon Based MEMS Materials and Technologies (Second Edition)*, Micro and Nano Technologies, pages 444 – 469. William Andrew Publishing, Boston, second edition edition, 2015. ISBN 978-0-323-29965-7. doi: <https://doi.org/10.1016/B978-0-323-29965-7.00021-X>. URL <http://www.sciencedirect.com/science/article/pii/B978032329965700021X>.
- [16] A. Lai and G. M. Cossu. High-resolution timing electronics for fast pixel sensors. *Journal of Instrumentation*, aug 2020. submitted for publication.
- [17] J. Lange et al. Radiation hardness of small-pitch 3d pixel sensors up to a fluence of $3 \times 10^{16} \text{ n}_{\text{eq}}/\text{cm}^2$. *JINST*, 13:P09009, 2018.

- [18] LHCb collaboration. Expression of Interest for a Phase-II LHCb Upgrade: Opportunities in flavour physics, and beyond, in the HL-LHC era. *CERN-LHCC-2017-003*, 2017.
- [19] LHCb collaboration. Physics case for an LHCb Upgrade II — Opportunities in flavour physics, and beyond, in the HL-LHC era. *CERN-LHCC-2018-027, LHCb-PUB-2018-009*, 2018.
- [20] LHCb collaboration. VELO Upgrade-II Framework Technical Design Report. *CERN-LHCb paper*, 2020. under preparation.
- [21] X. Llopert. The design of the timepix4 chip: a 230 kpixel and 4-side buttable chip with 200ps on-pixel time bin resolution and 15-bits of tot energy resolution, 2019. URL https://indico.cern.ch/event/788037/attachments/1946069/3233311/Xavi_Timepix4_ESE.pdf.
- [22] S. Parker et al. 3d - a proposed new architecture for solid-state radiation detectors. *NIM A395, 328-34*, 1997.
- [23] Parker, S.I. and Kok A., and Kenney C. and Jarron P. and Hasi J. and Despeisse M. and Da Via C. and Anelli G. Increased speed: 3d silicon sensors; fast current amplifiers. *IEEE Trans. Nucl. Sci.*, 58 (2), pp. 404-417, 2011.
- [24] Ramo, S. Currents Induced by Electron Motion. *Proceedings of the IRE*, vol. 27, no. 9, pp. 584-585, 1939. doi: 10.1109/JRPROC.1939.228757.
- [25] W. Riegler and G. A. Rinella. Time resolution of silicon pixel sensors. *Journal of Instrumentation*, 12 (11):P11017–P11017, nov 2017. doi: 10.1088/1748-0221/12/11/p11017. URL <https://doi.org/10.1088/1748-0221/12/11/p11017>.
- [26] H.-W. Sadrozinski et al. Ultra-fast silicon detectors (UFSD). *Nuclear Instruments and Methods in Physics Research Section A: Accelerators, Spectrometers, Detectors and Associated Equipment*, 831: 18 – 23, 2016. ISSN 0168-9002. doi: <https://doi.org/10.1016/j.nima.2016.03.093>. URL <http://www.sciencedirect.com/science/article/pii/S0168900216301279>. Proceedings of the 10th International Hiroshima Symposium on the Development and Application of Semiconductor Tracking Detectors.
- [27] Synopsys Inc. Synopsys Sentaurus TCAD Version 2018.06 K-2015.06, 2018. URL <https://www.synopsys.com/silicon/tcad.html>.